Cytometry
PART A
Journal of the
International Society for
Advancement of Cytometry

Reconstructing the Orientation Distribution of Actin Filaments in the Lamellipodium of Migrating Keratocytes from Electron Microscopy Tomography Data

Julian Weichsel,[1,2] Edit Urban,[3] J. Victor Small,[3] Ulrich S. Schwarz[1,2]*

[1]Bioquant, Heidelberg University, Heidelberg 69120, Germany

[2]Institute for Theoretical Physics, Heidelberg University, Heidelberg 69120, Germany

[3]Institute of Molecular Biotechnology, Vienna 1030, Austria

*Correspondence to: Ulrich S. Schwarz, Bioquant, Heidelberg University, Heidelberg 69120, Germany.

E-mail: ulrich.schwarz@bioquant. uni-heidelberg.de

ISAC
International Society for Advancement of Cytometry

• **Abstract**

Migration of motile cells on flat substrates is usually driven by the polymerization of a flat actin filament network. Theoretical models have made different predictions regarding the distribution of the filament orientation in the lamellipodium with respect to the direction of motion. Here we show how one can automatically reconstruct the orientation distribution of actin filaments in the lamellipodium of migrating keratocytes from electron microscopy tomography data. We use two different image analysis methods, an algorithm which explicitly extracts an abstract network representation and an analysis of the gray scale information based on the structure tensor. We show that the two approaches give similar results, both for simulated data and for electron microscopy tomography data from migrating keratocytes. For the lamellipodium at the leading edge of fast moving cells, we find an orientation distribution that is peaked at $+35/-35$ degrees. For the lamellipodium at the leading edge of slow moving cells as well as for the lamellipodium at the flanks of fast moving cells, one broad peak around 0 degree dominates the distribution. © 2012 International Society for Advancement of Cytometry

• **Key terms**

cell migration; keratocyte; lamellipodium; actin cytoskeleton; electron microscopy; digital image processing; orientation analysis

INTRODUCTION

The directed polymerization of filaments built from the structural protein actin is a generic propulsion mechanism used in very different biological systems of interest, ranging from immune cells to human pathogens [1]. During migration on flat substrates, motile cells usually generate a widely spread and thin, almost sheet-like lamellipodium at their advancing edge [2]. As a prerequisite for cell migration, such actin polymer networks generate the necessary work for protruding the cell membrane at the front by polarized growth against the leading edge [3].

Although a cell type-specific network of regulatory proteins determines the exact dynamics of the lamellipodium, a small subgroup of what is believed to be the key proteins of the process has been identified and appears to be conserved in many different situations [4,5]. This fact and the particular importance of mechanical aspects in understanding the propulsion mechanism has made this system a paradigm for biophysical modeling in recent years [6–8]. Many mathematical models focusing on different aspects of the process have been helpful in rationalizing and interpreting previously puzzling experimental results [9]. These models, however, are frequently challenged by the results of new experimental techniques accessing the subject in greater detail and yielding unexpected results [7,10,11].

Because most optical techniques up to date are not able to resolve the required details, electron microscopy (EM) is the most important type of experimental data which helps to understand the spatial organization of the lamellipodium [12]. Pioneering work by Borisy and coworkers suggested that the lamellipodium is organized in a surprisingly regular manner, with frequent branching junctions leading to an overall criss-cross pattern [13,14]. Recently, it has been shown with advanced EM techniques that the organization of the lamellipodium might be more variable, with less branching and more three-dimensional crosslinking [10,11,15]. The newly available EM data now open up the perspective to achieve more reliable and quantitative information than formerly possible, and to make interesting comparison with theoretical predictions.

In the past, different theoretical models have made interesting predictions for the spatial structure of the lamellipodium. Modeling the polymerization of a single filament against an external force yielded an optimum filament orientation for fastest growth at around $48°$ [16]. Later, Maly and Borisy suggested that two competing patterns exist due to a competition of branching and orientation dependent capping of filaments, with orientations peaked at $+35/-35$ and $+70/0/-70$ degrees [17]. Motivated by the available EM evidence, it was concluded that a pattern with peaks at $+35/-35$ degrees dominates in lamellipodia under physiological conditions, as also suggested by stochastic network simulations [18]. Introducing an orientation dependent branching rate in the model yielded similar $+35/-35$ degrees patterns as before, but with subdominant patterns adding more features to the orientation distribution histograms [19]. Recently it has been shown that the competition between the $+70/0/-70$ and $+35/-35$ degrees patterns leads to bistability and hysteresis effects [20]. Thus, these theoretical findings are able to explain puzzling experimental results including hysteresis effects in actin networks grown in vitro against an atomic force microscope cantilever [21].

To evaluate the experimental data quantitatively, appropriate image processing methods have to be developed. So far different routines have been used to deduce information on the network architecture of biological samples, like for instance astrocyte cell clusters [22] and intermediate filament networks [23]. Also actin filament networks have been analyzed and classified according to their structural organization [24,25]. Some approaches focused specifically on the actin network orientation from microscopy images of lamellipodia. A combination of filament edge segmentation and subsequent Radon transform [17,26] as well as a network model based image analysis [27] led to the conclusion that the dominant orientation distribution peaked at around $+35/-35$ degrees is the only relevant pattern in the physiological context. However, recently a correlated measurement of the leading edge velocity and subsequent manual orientation analysis of randomly selected single filaments demonstrated a substantial increase in the relative number of filaments oriented more parallel to the leading edge after transitions from protrusion to pause [28].

Here, we refine and automatize this correlated measurement approach by analyzing several two-dimensional (2D) slices of three-dimensional (3D) tomographic EM data of the lamellipodium network. To evaluate the orientation distribution of actin filament networks on EM images of the lamellipodium of motile keratocyte cells, we will rely on two different data analysis strategies. First, we will extract an abstract 2D actin network representation, consisting of nodes connected by straight line segments. This algorithm was customized for our specific type of EM data. Therefore, in order to yield accurate and correct results, the method requires a rather high image quality. The performance of this algorithm can be judged directly by visual comparison of the extracted networks to the raw image data and hence, a similar accuracy as observed is expected from the subsequent orientation analysis.

Second, we will discuss a gray value gradient based orientation measure based on the structure tensor calculus [25,29]. As this procedure evaluates the gray value gradients within a small neighborhood around each pixel of the image and extracts the desired orientation information from this calculus, it is applicable to a wide range of different images. Even if the resolution of the image is far lower than the typical length scale of the individual actin network constituents, this analysis can still yield informative results. Our main conclusion is that both methods give similar results, both for simulated and experimental data, and demonstrate clear differences between the actin filament orientation distributions of fast and slowly protruding parts of the lamellipodia.

MATERIALS AND METHODS

We performed experiments with motile fish keratocyte cells as described earlier [15,28,30], but now with a special focus on the role of growth velocity. Fish keratocytes were prepared from scales of freshly killed brook trout (*Salvelinus fontinalis*). Primary cultures of keratocytes, produced by incubating the fish scales in growth medium in plastic Petri dishes, were treated with trypsin and the released cells re-plated onto Formvar-coated electron microscope grids. The living cells were imaged under phase contrast optics in a Zeiss Axioscope inverted microscope and time lapse sequences recorded on a Micromax CCD camera (Roper Scientific) at time intervals of 5–10 seconds. After one of the motile cells slowed down, all cells were fixed by exchanging the growth medium for a fixation/extraction solution containing a mixture of Triton X-100 (0.75%) and glutaraldehyde (0.25%) in cytoskeleton buffer (10 mM MES buffer, 150mM NaCl, 5mM EGTA, 5 mM glucose, and 5mM $MgCl_2$, at pH 6.1). After 1 min in this mixture, the cells were postfixed in 2% glutaradehyde in the same buffer containing $1\mu g/ml$ phalloidin and stored in this solution at $4°C$ until use. For electron tomography, the grids were negatively stained in aqueous, 4% sodium silicotungstate (Agar Scientific) at pH 7, containing BSA-saturated colloidal gold and tomogram series collected in an FEI Polara electron microscope operating at 300 kV. Reprojections from the tilt series were generated using IMOD software from the Boulder Laboratory for 3D Electron Microscopy of Cells.
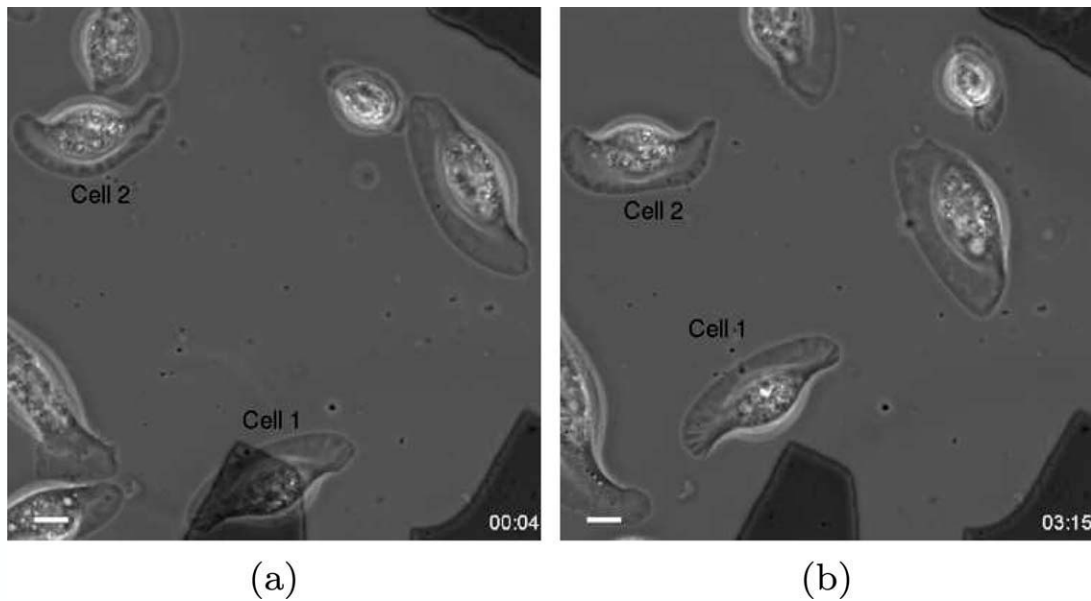
Reconstructing the Orientation Distribution of Actin Filaments

Figure 1. Two snapshots of a live-microscopy video of motile keratocyte cells at the beginning of the recorded movie (**a**) and just before the fixation of the cells (**b**). The time code of the individual images is displayed on the respective lower right corner in units of minutes and seconds. The two keratocyte cells that were analyzed in EM and image processed later are indicated on these images. Cell 1 moved steadily over the substrate at a relatively high velocity. Compared to its initial velocity, Cell 2 slowed down significantly just before fixation. Scale bar is 10 μm.

RESULTS

Live Cell Imaging and Tomography

Although we expect that changes in network velocity trigger transitions in the filament orientation distribution in the lamellipodium, this cannot be easily manipulated from the outside. In fact it is not sufficient to compare two cells crawling with different absolute velocities, because the important parameter that dictates network orientation is the protrusion speed measured relative to the single filament polymerization velocity [20]. As this polymerization speed itself depends on many intrinsic characteristics of the cell, like the available actin monomer concentration at the leading edge and regulatory circuits, it is an individual property of each cell. Hence, it is not unlikely that two cells, migrating at different speed, could still crawl in the same dynamic regime and with similar actin network organization.

To approach this problem, we utilized two different strategies. First, we used the fact that the velocity of individual cells crawling on a culture dish naturally varies due to random differences in the external and internal conditions for each cell. The analysis of correlated data from two different microscopy setups allowed us to exploit these stochastic variations and extract the structural organization of the actin network for different cell velocity and therefore protrusion speed of the leading edge network. Different moving fish keratocyte cells are observed in a live-microscope in real time. Once one cell slows down significantly, all cells are fixed in their present dynamical state. Subsequently, the lamellipodium network of the cells is analyzed in high resolution EM tomography. Although it is not possible to measure directly the network velocity relative to the active single filament polymerization speed in the

final state, we know from the live-cell images which cell slowed down just before fixation. Therefore it is likely that this cell switched its dynamical state at this point. From here on we can compare the network orientation distribution in this cell to another cell which was moving unperturbed at a relatively high velocity and compare the two for differences in the filament orientation patterns.

Second, we used the fact that protrusion rates and therefore presumably also actin network organization vary considerably along the boundary of a locomoting keratocyte, with a much smaller normal component at the flanks than at the front [31,32]. We therefore also performed analysis of EM data from different locations at the boundary of steadily moving cells, namely both at the center of the leading edge and at the sides.

In Figure 1, we show two snapshots from a live-microscopy video of motile keratocytes (see Supporting Information movie 1). The absolute velocities of the two cells marked on the images is not directly relevant for our considerations. However, it is important to note that Cell 1 moved steadily and with approximately constant velocity over the whole recording time, while Cell 2 has slowed down to the point where its cell body was only barely moving anymore. The important parameter for our analysis is the relative velocity of the leading edge with respect to filament polymerization, which we assume to be much smaller here compared to the steadily moving cell. After fixation and tomography reconstruction, all slices of the volumetric stack were preprocessed, before the actual filament network analysis started. Here, the contrast of all images was increased and bright prominent marker dots that are necessary for the reconstruction of the tomograph were removed from
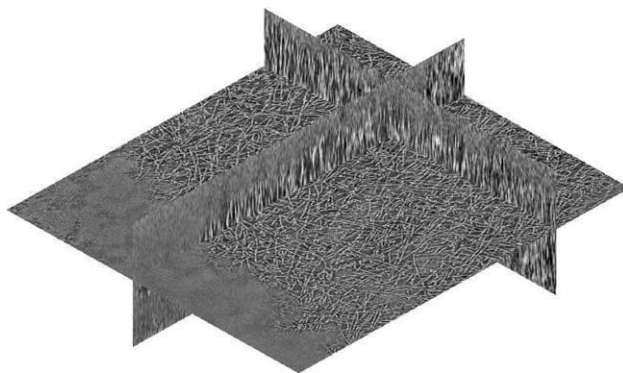
Figure 2. Plot of representative slices through a typical EM image data cube. The total volume of the image data is 1.3 μm $\times$ 1.2 μm $\times$ 0.1 μm.

the images. Figure 2 shows a slice plot through the image stack. It clearly demonstrates that relatively long segments of individual filaments lie in a single image z-plane parallel to the surface before they are leaving the focus of the slice (see also Supporting Information movie 2). This shows that the lamellipodium is essentially organized in two dimensions and validates our approach to conduct a 2D analysis.

Filament Network Extraction

We first developed a 2D network extraction algorithm suitable for our EM tomography slices of lamellipodium actin networks. A similar approach has been used successfully before to construct graphs from image data of astroglial cells in the central nervous system [22]. Despite the fact that in principle the network extraction routine described in the following could be generalized to 3D, here we restrict our approach to two dimensions. Our available EM data consists

of volumetric stacks of 2D slices through the lamellipodium parallel to the surface, at a position close to the leading edge of the cell. The lamellipodium is typically 200 nm thick, but several microns wide, and therefore effectively 2D. For the specific scope of this work, namely extracting projected filament orientation distributions, the 2D approach is therefore sufficient. To obtain other physical parameters from the extracted actin networks, like filament connectivity, a complete 3D network reconstruction would be required. Such a 3D network analysis has been carried out before for intermediate filament networks using a commercially available image processing package in combination with algorithms for artifact compensation [23].

The final goal of our 2D approach is to describe the complex 2D actin network structures by a graph consisting of located nodes and a connectivity matrix indicating which pairs of nodes are directly linked by linear (filament) line segments. In this way, we are efficiently reducing the experimental data to the information which is relevant for us, the filament orientation distribution. Although nodes between segments that are found by the algorithm might often only be artifacts but no physical crosslinks between filaments, due to the 2D projections of the 3D network, we are interested in the orientation of filament segments and thus this effect does not influence our results significantly. The algorithm for network extraction can be subdivided in the following five steps, segmentation, skeletonization, classification of nodes, graph creation, and network correction and simplification.

Segmentation. As a preparation for network extraction, the actin network visible on the EM image is segmented. This is a crucial step in the analysis as the final accuracy of this segmentation will have a significant impact on the quality of the results from later processing steps for network extraction. For
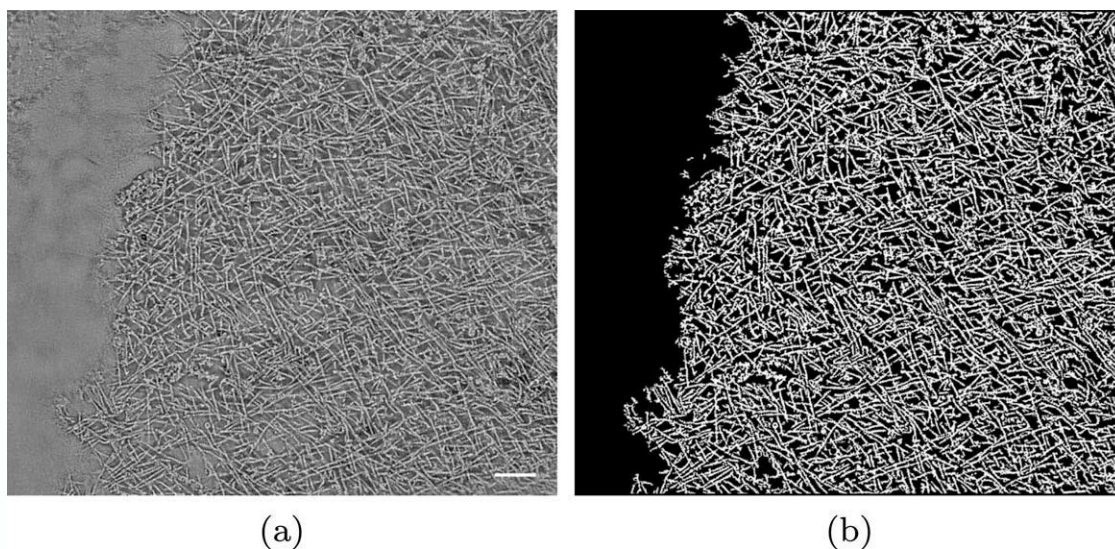

(a)

(b)

Figure 3. Segmentation of the actin network on a representative slice of EM tomography data obtained from the lamellipodium of a motile fish keratocyte cell. (**a**) Grayscale representation of one slice of the volumetric data reconstructed from EM tomography. Scale bar is 0.1μm. (**b**) Final black and white network image after binarization, removal of the background and smaller artifacts.
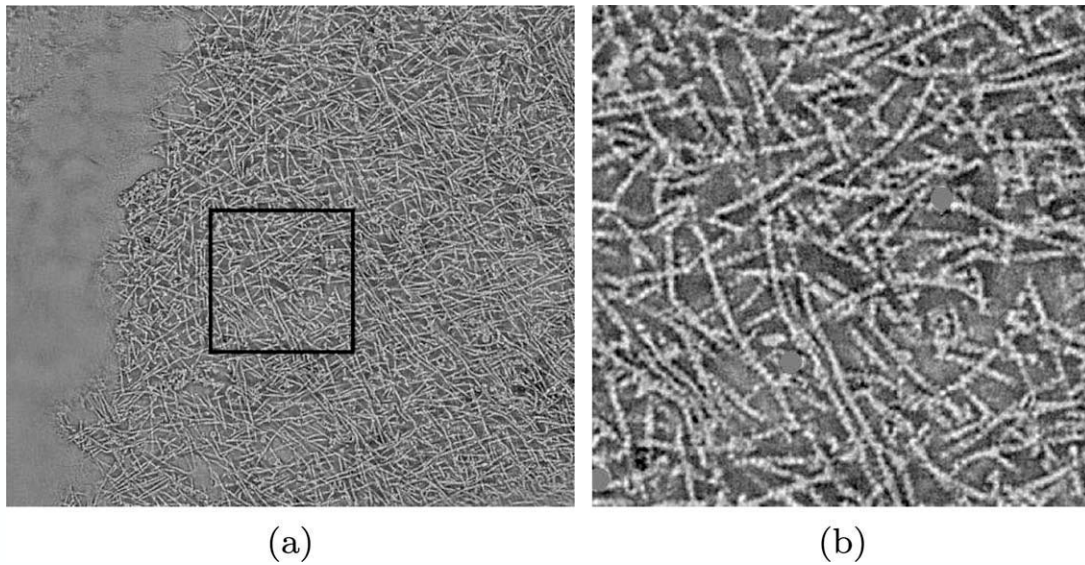
Figure 4. To keep the presentation of the network extraction algorithm illustrative, we will explain the analysis procedure by applying it to a smaller sample section of the full 2D sample slice. (**a**) Full EM slice, with the boundary of the smaller sample region indicated in black. (**b**) Magnified sample region from (a). One edge of the quadratic sample region spans 0.34 μm.

this reason it is not possible to apply this approach to low quality image data, as then it is very hard or often even impossible to reliably segment the network constituents in an automated procedure. As an alternative to an initial segmentation step, also other approaches exist which allow to simplify a grayscale image directly, while preserving its topology [35]. For 2D scanning electron microscope images, network characteristics of intermediate filaments have been successfully analyzed along these lines before [36].

For a good segmentation, i.e., a black and white representation of the actin network on the image, we first binarized the image using Otsu's method [37]. This primary segmentation however was imperfect due to artifacts outside the lamellipodium and between filaments. Therefore we needed to specify the bulk region occupied by the actin network in the image. As the EM images were taken in close proximity to the leading edge, not the whole image region was filled by the network. For this purpose, we evaluated the coherency measure for the images that have been noise reduced by median and Wiener filters before. Coherency is able to distinguish actin network structures from a uniform or noisy background [25]. A binarized version of the coherency feature image yielded a good estimate for the boundaries of the actin network in the 2D slices of the volumetric image stack. As an additional measure that is able to detect smaller holes in the actin mesh, where no filaments are present, we used the normalized square root of the trace of the structure tensor. This tensor had already been calculated before to obtain the coherency. After applying a maximum filter and subsequent binarization, we got the relevant network region in the image, in which filaments were actually present. Pixelwise multiplication of the three binarized images, i.e. the one obtained from Otsu's method, the binarized coherency and the binarized trace of the structure

tensor yielded a preliminary result for the segmented network. In a last step, we analyzed this image for small artifacts, i.e., separated clusters of pixels with a total area smaller than a given threshold, which were then deleted. This completed the segmentation process. A representative original image is shown in Figure 3a, together with its segmented version in (b). In the following, to give a detailed impression on how the network extraction procedure performs on EM images, we will illustrate individual analysis steps on a small region of the large sample image. Figure 4 indicates this smaller cutout from the sample EM slice.

Skeletonization. We begin the network extraction starting from the black and white version of the filament network, that is cut from the binarized full image as shown in Figure 5a. First, a thinning or skeletonization algorithm is applied. In this step, the width of all segmented objects is iteratively reduced to a final thickness of one pixel, without altering the connectivity of the binary image. The final skeletonization result is displayed in Figure 5b.

Classification of nodes. At this point, the width of all objects in the image is exactly one pixel and therefore it is possible to classify endpoints of objects as nodes. Endpoints are defined as white pixels with exactly one other white pixel in their direct neighborhood defined by eight surrounding pixels. In Figure 5c such endpoints are marked in red. As we disregard single isolated white pixels, every endpoint is connected to at least one other endpoint by a closed path of white pixels. However, it is also possible that a single endpoint is linked to more than one other endpoints, if the connecting white path starting at its position splits up on the way. Hence, we define a
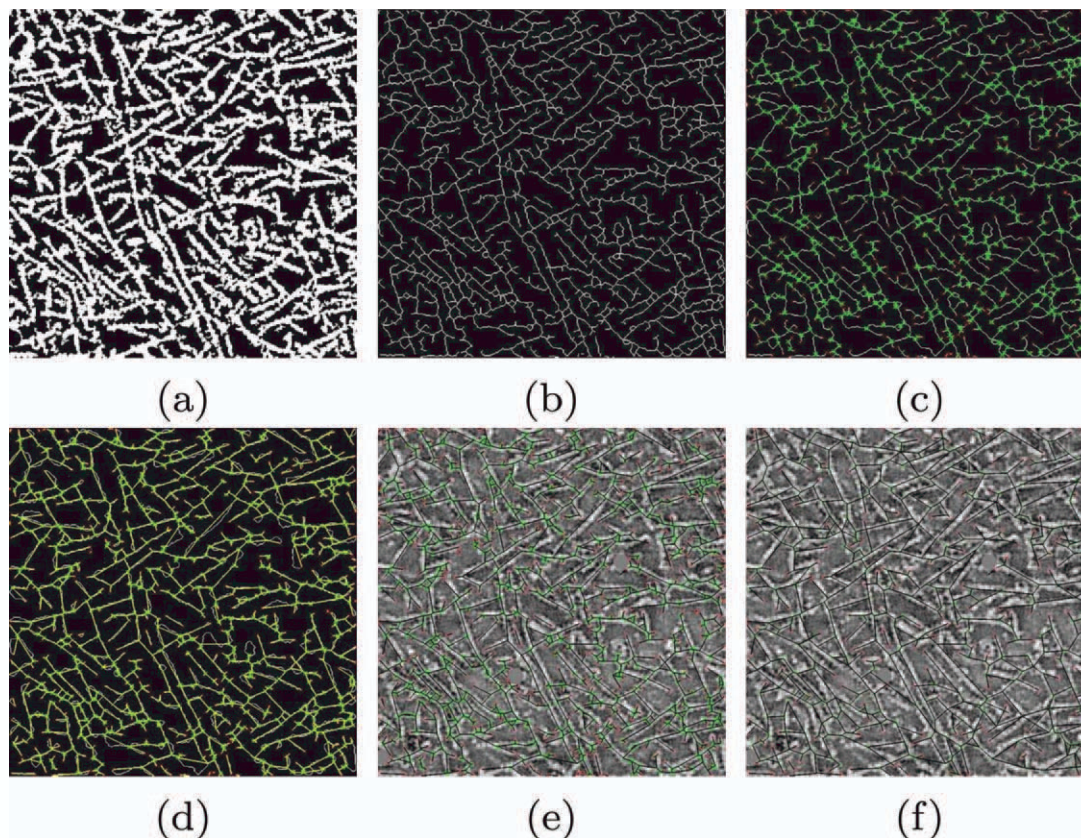
Figure 5. Sequential steps of the network extraction routine. (**a**) Sample region of the binarized 2D EM image as indicated in Figure 4. (**b**) Segmented region after skeletonization. The connectivity of segmented objects is not altered in this operation. (**c**) Nodes are located and classified according to the number of white pixels in their direct neighborhood. Red nodes indicate endpoints, while green nodes indicate higher order nodes. (**d**) An adjacency matrix is constructed, that incorporates which nodes are directly connected by a continuous path of white pixels. An abstract network according to straight links between connected nodes is shown in yellow. (**e**) The same graph as in (d) is plotted on top of the original sample section of the gray value EM image for comparison. (**f**) The extracted network is simplified and corrected to some extend. Unnecessary nodes, short dead ends and small loops are removed, while potential gaps in line segments are bridged. The area of the quadratic sample region spans 0.34 μm $\times$ 0.34 μm. [Color figure can be viewed in the online issue, which is available at wileyonlinelibrary.com.]

second class of nodes at the position of these split-ups. Such higher order nodes or crosslinks are defined as white pixels with at least three other white pixels in their direct neighborhood. Higher order nodes are marked in green in Figure 5c.

Graph creation. Next, it is possible to construct a graph or network by tracing connected paths sequentially starting at all nodes which have been classified in the previous step. The result of this procedure is essentially an adjacency matrix. This quadratic matrix holds as many columns as nodes were found in the previous step and all of its entries are initially set to zero. If a connection is established between two nodes with indices i and j, the i, j-th element of the matrix is set to one. As links between nodes are undirected, only the upper triangle of the symmetric matrix has to be considered. In this way, we complement extracted nodes at certain positions in the image with the additional information, if pairs of nodes are connected. In other words, we have already extracted a primary network from the segmented image. This rudimentary network representation is shown in Figures 5d and 5e. To be able

to judge the accuracy of the extracted abstract linearized network compared to the original actin filament network, the skeletonized binary image and the sample section of the gray value EM image are shown in the background of the plots, respectively.

Network correction and simplification. The preliminary network holds a rather large number of unnecessary nodes, that does not contribute significantly to its architecture nor the segment orientation distribution. Additionally, imperfections in the segmentation process lead to artificial disconnections in filaments. Therefore, we implemented an additional correction and simplification routine for the primary extracted network.

Due to the specifics of the skeletonization algorithm we are using, multiple higher order nodes are often located in their direct neighborhood. Merging these clusters efficiently reduces the total number of nodes and therefore the dimension of the adjacency matrix. A new node, representative for the whole cluster, is positioned at the centerpoint of all nodes
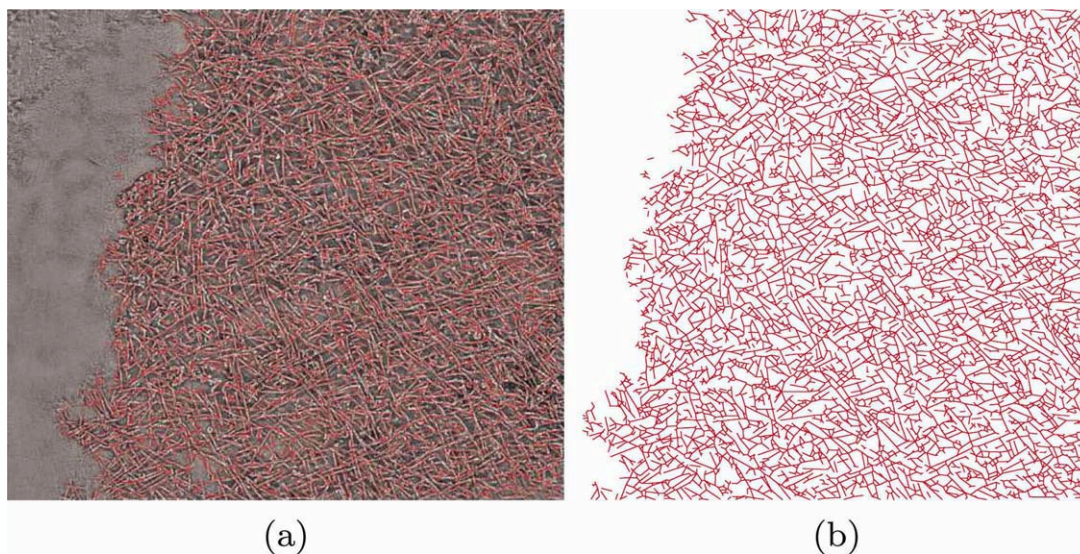
Figure 6. Extracted abstract fiber network as the result of the network extraction algorithm described in the main text and in Figure 5. (**a**) For better judgment of the quality of the resulting network, the original gray value EM image is shown in the background. (**b**) Plot of the extracted network exclusively. The scale of these images is defined as in Figure 3. [Color figure can be viewed in the online issue, which is available at wileyonlinelibrary.com.]

which were merged and accumulates all connections to outside nodes.

From Figure 5e it is also evident that the extracted network incorporates many rather short dead ends. Either these line segments do not correspond to filaments in the gray value image at all or represent filaments that were disconnected due to artifacts in the original image or due to an imperfect segmentation. Therefore, we correct for such dead ends in the following way: First, short dead ends are detected in the network as line segments that are shorter than a given threshold, while connecting at least one endpoint with an arbitrary node. Subsequently, the algorithm extrapolates these segments at their endpoint and connects them to other dead ends which are oriented similarly and located close to the extrapolated path. In this way small gaps in filaments are bridged. If a connection to another line segment is not likely, the dead end is classified as an artifact and deleted from the network.

An additional artifact of the skeletonization is the appearance of very small loops in the network. Therefore, we are tracing the network for such rather small loops, using a depth first search algorithm up to a maximum segment path length. Once a loop is detected, all involved nodes are merged to a single node located in their center, which also accumulates all of the connections to outside nodes.

As a last step, second order nodes, only connected to exactly two other nodes in the network, are analyzed for their importance. Such second order nodes might appear as a result of one of the simplification steps. If the change in orientation of the two connections at the position of such a node is smaller than a predefined threshold, the node is removed and the two connected nodes are linked directly.

For our example region, the final network after correction and simplification is shown in Figure 5f. Figure 6 shows the

abstract fiber network extracted from the full sample slice of the EM data.

Gray Value Gradient-Based Orientation Analysis

As an alternative to the network extraction algorithm, we also implemented an orientation analysis based on the structure tensor [29]. We have utilized this approach successfully before in the biological context to classify actin network architecture on high-throughput fluorescence microscopy data [25]. Briefly, a strategy to extract a unit vector $\hat{n}$ defining the local orientation in a small region of the image is to assume, that it deviates least from the gradient direction of the image gray values, $\nabla g(\vec{x})$. For this purpose, a promising procedure is to maximize,

$$(\hat{n} \cdot \nabla g(\vec{x}))^2 = |\nabla g(\vec{x})|^2 \cos^2(\measuredangle(\nabla g(\vec{x}), \hat{n})). \qquad (1)$$

Within a finite region, this amounts to an extremum principle,

$$\int_{-\infty}^{+\infty} w(\vec{x} - \vec{x}')(\hat{n} \cdot \nabla g(\vec{x}'))^2 \, d^2x' \rightarrow \max, \qquad (2)$$

where $w(\vec{x} - \vec{x}')$ is a window function, defining the neighborhood around pixel $\vec{x} = (x, y)$. To formulate these mathematical considerations, the discrete gray values of the image were considered as a scalar field $g(\vec{x})$, continuous in position and magnitude. For the analysis, we will express the necessary mathematical operators by 2D filter masks that are suitable to transfer our derived expressions to the quantized gray value images. The optimization problem can be solved by rewriting Eq. (2) as,
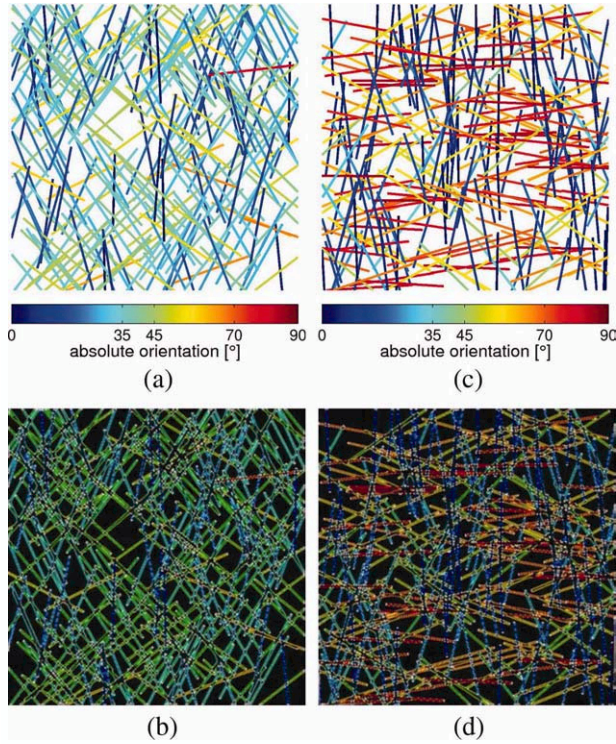
Figure 7. Orientation analysis of two realizations of random fiber networks using the structure tensor calculus. (**a**) and (**c**): Two examples of random fiber networks according to a +35/−35 (a) and a +70/0/−70 degrees (c) distribution. The orientation of the individual filaments is color labeled. (**b**) and (**d**): Feature images of the orientation, that were extracted using the structure tensor analysis of black and white versions of (a) and (c). The colorbars shown apply to all four images. To obtain such illustrative example images, the size of the window function (i.e., Gaussian filter) was reduced compared to the later analysis to obtain relatively sharp feature representations of the individual fibers. [Color figure can be viewed in the online issue, which is available at wileyonlinelibrary.com.]

$$\hat{n}^T \mathbf{J} \hat{n} \to \max, \qquad (3)$$

where the structure tensor **J** is defined as,

$$J_{pq}(\vec{x}) = \int_{-\infty}^{+\infty} w(\vec{x} - \vec{x}') \left(\frac{\partial g(\vec{x}')}{\partial p} \frac{\partial g(\vec{x}')}{\partial q} \right) d^2x'. \qquad (4)$$

This is a symmetric, positive semidefinit matrix and therefore there exist two orthogonal eigenvectors with non-negative eigenvalues. Hence, a suitable coordinate rotation reduces **J** to a diagonal matrix and the optimization problem reads,

$$\begin{bmatrix} \hat{n}'_x & \hat{n}'_y \end{bmatrix} \begin{bmatrix} J_{x'x'} & 0 \\ 0 & J_{y'y'} \end{bmatrix} \begin{bmatrix} \hat{n}'_x \\ \hat{n}'_y \end{bmatrix} \to \max. \qquad (5)$$

If both eigenvalues are equal, i.e., $J_{x'x'} = J_{y'y'}$, there is no dominant orientation observed in this neighborhood. Therefore, without loss of generality, we can assume $J_{x'x'} > J_{y'y'}$ and hence $\hat{n}' = \begin{bmatrix} 1 & 0 \end{bmatrix}$ maximizes Eq. (5) with maximum value $J_{x'x'}$. This means that in the coordinate system in which the structure tensor **J** is diagonal, i.e., the coordinate system spanned

by the two orthogonal eigenvectors of the matrix **J**, $\hat{n}$ and therefore the local orientation is given parallel to the eigenvector with the largest eigenvalue.

As an example, Figure 7 shows a representative extraction of a feature image from two different variants of a computer generated random fiber network. These random fiber networks have been used before to model mechanical characteristics [33] and transport properties [34] of biopolymer networks, but also to benchmark image processing routines for microscopy data of actin [25]. To obtain a realization of the stochastic network model, the positions of a constant number of fibers are chosen uniformly randomly within a confined 2D domain. Subsequently, the orientation angle of each fiber is randomly selected from a specified orientation distribution. Connections in the network are formed when two fibers happen to cross each other. For testing the extraction of fiber orientation distributions with our approaches, the connectivity of the fibers is of minor importance for low to moderate fiber densities; only at high fiber density, the large number of connections makes it difficult to resolve single fibers in the network. Reconsidering the model predictions for the structural organization of lamellipodium actin networks in [17,20], we expect two fiber orientation patterns to be especially relevant. Therefore at this point we draw fiber orientations from two different linear combinations of Gaussian distributions with means at either +35/−35 (Figs. 7a and 7b) or +70/0/−70 degrees (Figs. 7c and 7d), each with constant standard deviation $\sigma = 15°$. In the case of +35/−35 degrees networks, the weight of both peaks is chosen equal, while for the second +70/0/−70 degrees pattern, the weight of the peak at 0° is chosen twice as large as the constant weight at +70/−70 degrees. For illustration the absolute orientation of each fiber relative to the vertical boundary of the network is color coded in these images as indicated by the colorbar.

The lower two images in Figure 7 show results of the structure tensor analysis applied to gray scale representations of the network examples above using a feature image representation. The color in each pixel indicates its local orientation, while the saturation is given by the coherency measure,

$$c_c = \left(\frac{J_{x'x'} - J_{y'y'}}{J_{x'x'} + J_{y'y'}} \right)^2 = \frac{(J_{yy} - J_{xx})^2 + 4J_{xy}^2}{(J_{xx} + J_{yy})^2}, \qquad (6)$$

and the intensity by the trace of the structure tensor,

$$\mathrm{Tr}\,\mathbf{J} = J_{xx} + J_{yy} = J_{x'x'} + J_{y'y'}. \qquad (7)$$

This is a variant of the HSV-colorspace with a constraint hue domain. Colored pixels in the image indicate regions of clear orientation, while black pixels mark the uniform background without any dominant orientation. With regard to visual inspection the feature images appear to capture the original fiber orientation of their individual sample images reasonably well. In the following section, we will quantify this impression by calculating fiber orientation distributions from such random fiber networks and compare them to the actual
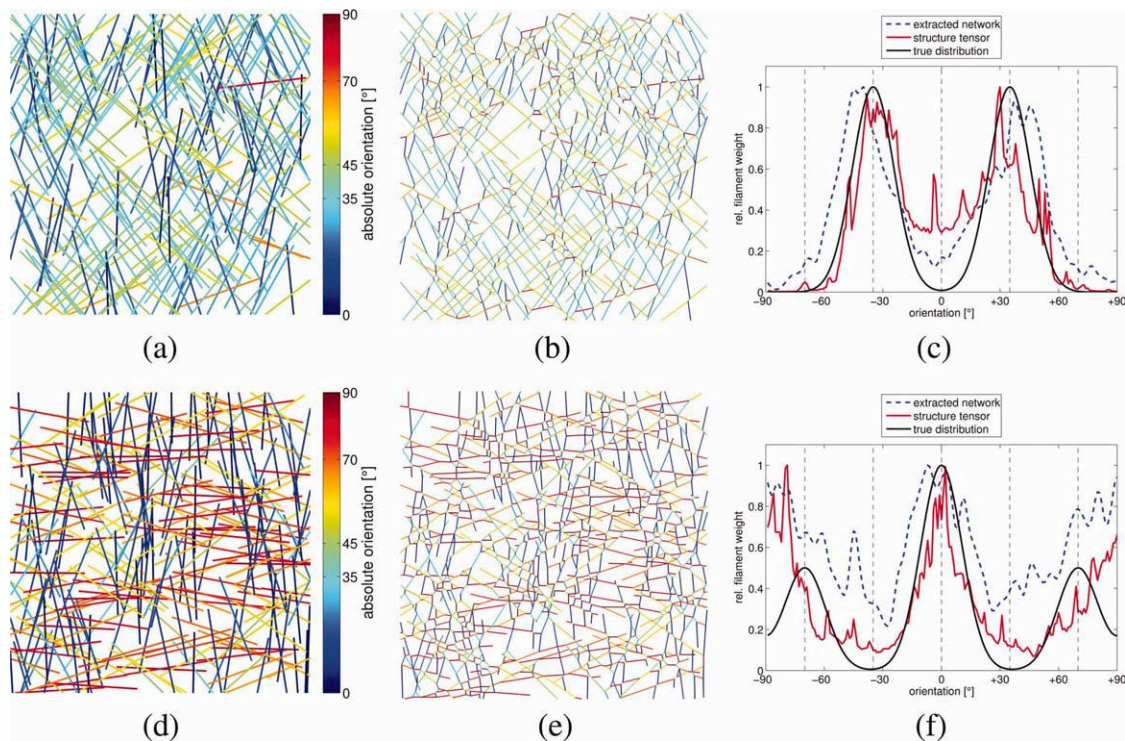
Figure 8. Orientation analysis of random fiber networks using network extraction and structure tensor calculus. (**a**) and (**d**): Two realizations of the random fiber networks. The model orientation distributions are either peaked at +35/−35 (a) or +70/0/−70 degrees (d), as indicated by the black curve in (**c**) and (**f**), respectively. (**b**) and (**e**): Extracted filament networks for the two sample networks above. (**c**) and (**f**): Resulting filament orientation distributions extracted from the networks according to our two independent approaches, using the structure tensor analysis (red line) and the network extraction routine (dashed blue line). The true distribution that was used during random fiber creation is shown as a benchmark (black line). [Color figure can be viewed in the online issue, which is available at wileyonlinelibrary.com.]

orientation probability distributions from which the ensemble of fibers has been drawn.

Analysis of Simulated Random Fiber Networks

To benchmark the accuracy of our two different image processing routines for extracting filament orientation patterns, we processed the two realizations of the computer generated random fiber model introduced earlier in "Gray Value Gradient-Based Orientation Analysis" Section. The line of reference for color labeling the fiber orientations in Figures 8a and 8d is assumed vertically, parallel to the lateral boundaries of the network like before. As can be roughly estimated by eye from this color labeling, the network in (a) was randomly created to simulate a +35/−35 degrees pattern, while a complementary +70/0/−70 degrees distribution is visible in (d). In (b) and (e) the extracted filament networks for the two examples are shown. The network extraction procedure was applied to a binarized version of the random fiber networks in (a) and (d) and subsequently extracted filament segments were color coded according to their individual absolute orientation. Extracted orientation distributions for the two simulated networks from our two independent approaches are shown in (c) and (f). To evaluate this distribution from an extracted network, the orientation of each line was considered as a small Gaussian with standard deviation $\sigma = 3°$ weighted by the

corresponding segment length. In case of the structure tensor the evaluated orientation at each pixel was considered and weighted by the coherency measure c_c at this position. The full distribution was subsequently convolved with a Gaussian filter of size $12°$ and $\sigma = 4°$ to average out fluctuations. All applied methods are able to recover the original fiber orientation distribution of the random networks to a similar, reasonably high extend. The major difficulty arises in the large angle domain of the +70/0/−70 degrees pattern. This is due to the limited separation of the +70/−70 degrees peaks. As the orientation of filaments is only defined in an angle domain modulo $180°$, the orientation difference between these peaks is only $40°$. It turns out, that the resolution of the applied analysis is not sufficiently high to clearly resolve those two separated Gaussians.

Analysis of Lamellipodia Networks

Finally, the two independent automated orientation analysis routines, i.e. network extraction and gradient based structure tensor calculus, were applied to stacks of EM images obtained experimentally. In case of the structure tensor routine, the preprocessed images were filtered with a median filter to reduce noise before analysis. Results from network extraction with color labeled orientation relative to a line perpendicular to the leading edge are shown in Figures 9b and 9e. The leading edge orientation is indicated as a separate black dashed
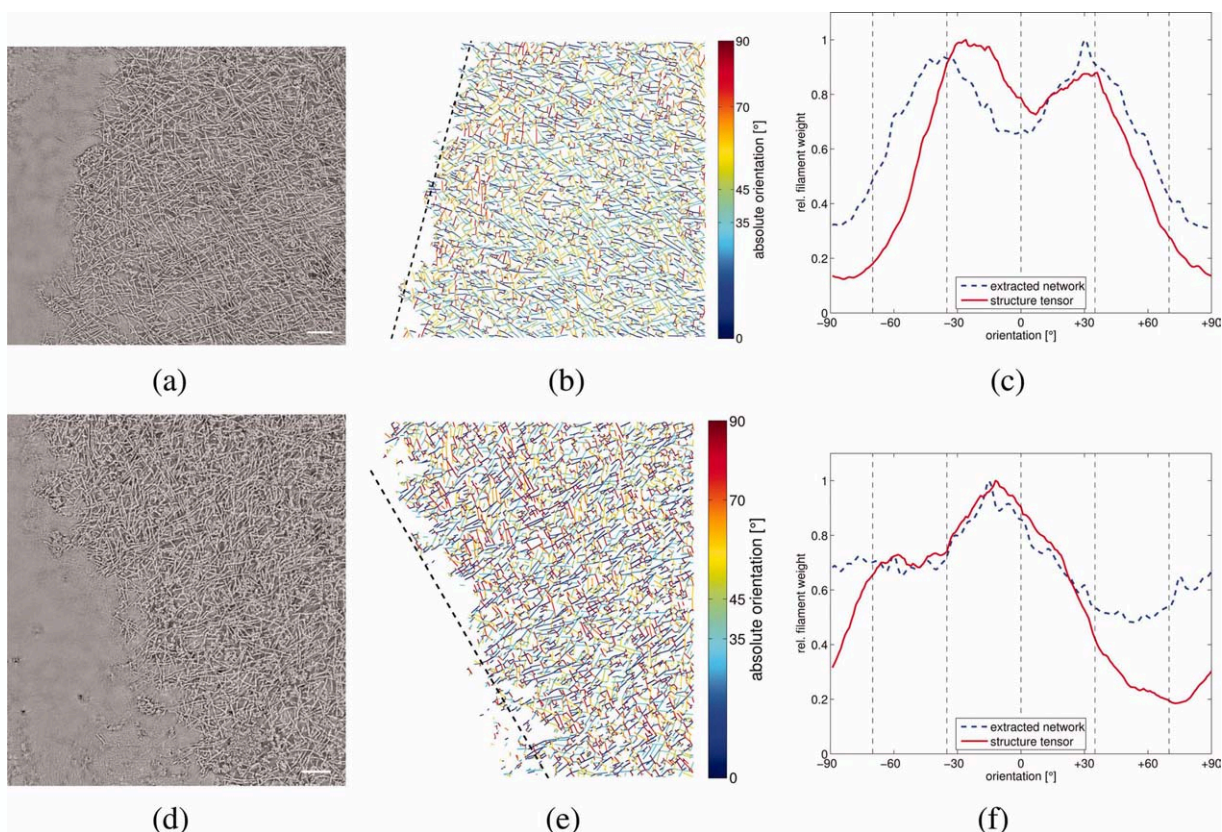
Figure 9. Representative slices of the EM tomograph and subsequent analysis results. The upper images correspond to Cell 1 (fast) and the lower images to Cell 2 (slow) as indicated in Figure 1. (a) and (d): Representative slices of the original data stack after preprocessing. Scale bar is 0.1 μm. (b) and (e): Extracted 2D filament segments from these images plotted in color coded orientation. (c) and (f): Orientation distributions of the two independent analysis methods averaged over twenty slices of the complete stack (i.e., 20 × 0.746 nm = 14.92 nm). Results from the structure tensor calculus are red and from filament network extraction are dashed blue. [Color figure can be viewed in the online issue, which is available at wileyonlinelibrary.com.]

line. This leading edge orientation was fitted manually to the stack and held as a constant reference orientation for the complete stack.

The final results for the orientation distribution of the filaments in the lamellipodium networks are shown in Figures 9c and 9f for Cell 1 and Cell 2 (compare Fig. 1). To obtain these distributions, we averaged over twenty adjacent slices in the middle of each stack, where the lamellipodium network appeared to be best visible without artifacts from the upper or lower boundaries. The tomograph voxels are cubic and so the spacing in z-direction is equal to the lateral dimensions, 0.746 nm. Therefore, in total we are averaging over around 14.92 nm in z. Considering typical actin filament diameters around 7 nm, this means that we take into account filaments from at least two independent layers of actin and so the results are not only locally representative but rather for a reasonable fraction of the bulk network. This analysis shows, that the actin network protruding in the steadily moving Cell 1 features a prominent orientation pattern around +35/−35 degrees. In marked contrast, Cell 2, which has slown down before fixation, yields a qualitatively different distribution. First, this orientation pattern spreads to broader angles more parallel to the front as already indicated in [28] and second, a single peak

is observed within an angle domain near perpendicular to the leading edge. Although peaks at +70/−70 degrees are not detected, as would be expected from the theoretical predictions [20], this might be attributed to the close proximity of these populations in orientation space modulo 180° as it was observed for the analysis of artificially created random fiber networks before in Figure 8 ("Analysis of Simulated Random Fiber Networks" section). In general, the +35/−35 degrees pattern is expected to always give a clearer signature than the +70/−70 degrees pattern.

The results from the two independent image analysis procedures shown in Figure 9 demonstrate a clear difference in the orientation patterns of the fast and slow moving cells. However, there are also clear differences between the results from the different algorithms, especially for the slower cell at large filament orientations. The strong asymmetry of the orientation distribution extracted with the structure tensor might have different reasons, including a stochastic fluctuation in network growth (compare the simulated realizations in Figure 8, which also lead to asymmetries), the corrugation in the nearby cell edge, or some artifact resulting from the algorithm. In general, the two procedures developed here are very different in nature. Although the network extraction routine

exclusively accounts for the filament orientation of segments that have been explicitly identified due to their large contrast, the structure tensor averages orientations over all grayvalue gradients within the network region. Future work is required to determine which of the two algorithms gives a more reliable presentation of the actin filament orientations, but both agree in demonstrating a clear difference between fast and slow cells.

The same results were obtained for EM data sets taken from different locations along the cell boundary of steadily moving cells (additional data given in Supporting Information). Three additional data sets were analyzed from the front of the lamellipodium. These networks feature the same criss-cross filament orientation pattern as the steadily moving Cell 1 in Figure 9. Then two additional data sets were analyzed from the lateral flanks of the lamellipodium, where protrusion in the locally orthogonal direction is diminished. Here, qualitatively different filament orientation distributions emerge, which feature a single dominant peak approximately orthogonal to the local orientation of the cell membrane. Therefore slowly protruding parts of the lamellipodium of a fast moving cell are organized in a similar manner than the lamellipodium at the leading edge of the slow moving cell in Figure 9.

DISCUSSION

The actin filament orientation distribution is a key quantity to understand how the lamellipodium performs its function. Here we have described a quantitative approach to extract this orientation distribution for the lamellipodium of locomoting keratocytes and found that two distinctly different patterns emerge for fast versus slowly protruding networks. In particular, we find that the leading edge of slowly moving cells and the flanks of fast moving cells show the same broad orientation distribution, in contrast to the leading edge of fast moving cells, which show the well known criss-cross pattern of fast growing networks.

We have developed two independent data analysis methods for the orientation analysis of the lamellipodium EM data. Both procedures work mostly automated with only minor or no manual adjustments necessary. On the microscopic level, we have implemented a network extraction algorithm which generates abstract graph representations of the underlying actin networks. The quality of the resulting artificial networks can be tested directly by visual comparison to the original gray value EM images. On a more macroscopic level, we have used an established gradient based structure tensor analysis. This method does not incorporate any a priori knowledge that could bias the resulting orientation distributions.

We tested our analysis with artificially created random fiber networks for the two different orientation patterns that have been theoretically predicted before. The two approaches were able to reliably distinguish the two patterns and extract a reasonable estimate for the underlying original distribution. Applying our analysis to experimental data, we measured and analyzed actin networks in the lamellipodia of two different fish keratocyte cells. One was moving steadily while the other slowed down just before fixation. Both independent analysis methods yielded similar results on each of these two sample cells. The resulting orientation distributions were averaged

over 20 subsequent slices of the volumetric EM data. For the fast cell, a dominant distribution with peaks around $+35/-35$ degrees was measured, which could be attributed to a cell moving in a medium growth phase dynamic regime as predicted theoretically in [20]. The second perturbed cell featured a broad distribution with a dominant peak at an orientation almost orthogonal to the leading edge. This hints at a cell moving in a different regime, termed slow growth phase in the theoretical description. Secondary peaks at $+70/-70$ degrees which would be expected from the model were not observed. However, this could be attributed to the limited resolution of the two methods as confirmed by the analysis of artificial random fiber networks. Our conclusions were verified by an additional analysis using EM data sets from different locations along the boundary of steadily moving cells. This showed that the slowly protruding regions at the flanks of fast moving cells have a similar actin orientation distribution like the front regions in slowly moving cells. Future experiments have to show if the obtained results can be confirmed for larger cell populations.

Our representative orientation analysis results fit very well to previously published experimental data, where changes in the filament orientation of mouse melanoma cells have been correlated to the speed of lamellipodium protrusion [28]. In this study, it was also observed that the orientation distribution broadens for slower velocities of the leading edge. The dominant $+35/-35$ degrees pattern, that has been observed in the steadily moving cell, has also been reported previously in Refs. 17 and 26. The methods developed here now set the ground to evaluate the actin filament orientation distribution in migrating cells for a larger number of data sets and for systematically varied conditions. In the long run, this might allow us to clearly discriminate between different model predictions.

LITERATURE CITED

1. Carlier MF, editor. Actin-Based Motility. Dordrecht: Springer; 2010.
2. Small JV, Stradal T, Vignal E, Rottner K. The lamellipodium: Where motility begins. Trends Cell Biol 2002;17:109–118.
3. Pollard TD, Borisy GG. Cellular motility driven by assembly and disassembly of actin filaments. Cell 2003;112:453–465.
4. Loisel TP, Boujemaa R, Pantaloni D, Carlier MF. Reconstitution of actin-based motility of listeria and shigella using pure proteins. Nature 1999;401:613–616.
5. Stuhrmann B, Huber F, and Käs J. Robust organizational principles of protrusive biopolymer networks in migrating living cells. PLoS One 2011;6:e14471.
6. Mogilner A. On the edge: Modeling protrusion. Curr Opin Cell Biol 2006;18:32–39.
7. Mogilner A. Mathematics of cell motility: have we got its number? J Math Biol 2009;58:105–134.
8. Pollard TD, Berro J. Mathematical models and simulations of cellular processes based on actin filaments. J Biol Chem 2009;284:5433–5437.
9. Carlsson AE, Mogilner A. Mathematical and physical modeling of actin dynamics in motile cells. In: Carlier MF, editor. Actin-Based Motility. Dordrecht: Springer; 2010. pp 381–412.
10. Small JV. Dicing with dogma: De-branching the lamellipodium. Trends Cell Biol 2010;20:628–633.
11. Ydenberg CA, Smith BA, Breitsprecher D, Gelles J, Goode BL. Cease-fire at the leading edge: new perspectives on actin filament branching, debranching, and cross-linking. Cytoskeleton 2011;68:596–602.

12. Baumeister W. Electron tomography: Towards visualizing the molecular organization of the cytoplasm. Curr Opin Struct Biol 2002;12:679–684.

13. Svitkina TM, Verkhovsky AB, McQuade KM, Borisy GG. Analysis of the actin–myosin II system in fish epidermal keratocytes: Mechanism of cell body translocation. J Cell Biol 1997;139:397–415.

14. Svitkina TM, Borisy GG. Arp2/3 complex and actin depolymerizing factor/cofilin in dendritic organization and treadmilling of actin filament array in lamellipodia. J Cell Biol 1999;145:1009–1026.

15. Urban E, Jacob S, Nemethova M, Resch GP, Small JV. Electron tomography reveals unbranched networks of actin filaments in lamellipodia. Nat Cell Biol 2010;12:429–435.

16. Mogilner A, Oster G. Cell motility driven by actin polymerization. Biophys J 1996;71:3030–3045.

17. Maly IV, Borisy GG. Self-organization of a propulsive actin network as an evolutionary process. Proc Natl Acad Sci USA 2001;98:11324–11329.

18. Schaus TE, Taylor EW, Borisy GG. Self-organization of actin filament orientation in the dendritic-nucleation/array-treadmilling model. Proc Natl Acad Sci USA 2007;104:7086–7091.

19. Quint DA, Schwarz JM. Optimal orientation in branched cytoskeletal networks. J Math Biol 2011;63:735–755.

20. Weichsel J, Schwarz US. Two competing orientation patterns explain experimentally observed anomalies in growing actin networks. Proc Natl Acad Sci USA 2010;107:6304–6309.

21. Parekh SH, Chaudhuri O, Theriot JA, Fletcher DA. Loading history determines the velocity of actin-network growth. Nat Cell Biol 2005;7:1219–1223.

22. Braumann UD, Franke H, Hengstler J, Kuska JP, Weber M.Graph-based quantification of astrocytes. In: Proceedings of the Bildverarbeitung für die Medizin, 19–21 March 2006, Hamburg, Germany. Handels H, Ehrardt J, Horsch A, Meinzer H-P, Tolxdorff T, editors. 2006; pp 379–383.

23. Lück S, Sailer M, Schmidt V, Walther P. Three-dimensional analysis of intermediate filament networks using SEM tomography. J Microsc 2010;239:1–16.

24. Fleischer F, Ananthakrishnan R, Eckel S, Schmidt H, Käs J, Svitkina T, Schmidt V, Beil M. Actin network architecture and elasticity in lamellipodia of melanoma cells. New J Phys 2007;9:420.

25. Weichsel J, Herold N, Lehmann MJ, Kräusslich HG, Schwarz US. A quantitative measure for alterations in the actin cytoskeleton investigated with automated high-throughput microscopy. Cytom Part A 2010;7A:52–63.

26. Verkhovsky AB, Chaga OY, Schaub S, Svitkina TM, Meister JJ, Borisy GG. Orientational order of the lamellipodial actin network as demonstrated in living motile cells. Mol Biol Cell 2003;14:4667–4675.

27. Schaub S, Meister JJ, Verkhovsky AB. Analysis of actin filament network organization in lamellipodia by comparing experimental and simulated images. J Cell Sci 2007;120:1491–1500.

28. Koestler SA, Auinger S, Vinzenz M, Rottner K, Small JV. Differentially oriented populations of actin filaments generated in lamellipodia collaborate in pushing and pausing at the cell front. Nat Cell Biol 2008;10:306–313.

29. Jähne B. Digital Image Processing. Berlin: Springer; 1997.

30. Auinger S, Small JV. Correlated light and electron microscopy of the cytoskeleton. Method Cell Biol 2008;88:257–272.

31. Fournier MF, Sauser R, Ambrosi D, Meister JJ, Verkhovsky AB. Force transmission in migrating cells. J Cell Biol 2010;188:287–297.

32. Barnhart EL, Lee K-C, Keren K, Mogilner A, Theriot JA. An adhesion-dependent switch between mechanisms that determine motile cell shape. PLoS Biol 2011;9:e1001059.

33. Wilhelm J, Frey E. Elasticity of stiff polymer networks. Phys Rev Lett 2003;91:108103.

34. Greulich P, Santen L. Active transport and cluster formation on 2d networks. Euro Phys J E 2010;32:191–208.

35. Couprie M, Bezerra FN, Bertrand G. Topological operators for grayscale image processing. J Electron Imaging 2001;10:1003–1015.

36. Lück S, Fichtl A, Sailer M, Joos H, Brenner R, Walther P, Schmidt V. Statistical analysis of the intermediate filament network in cells of mesenchymal lineage by greyvalue-oriented image segmentation. Comput Stat 2011; DOI: 10.1007/s00180-011-0265-1.

37. Otsu N. A threshold selection method from gray-level histogram. IEEE Trans Syst Man Cybern 1979;9:62–66.

Reconstructing the Orientation Distribution of Actin Filaments